Final Draft
of the original manuscript:

Steglich, D.; Brocks, W.; Heerens, J.; Pardoen, T.:
Anisotropic ductile fracture of Al 2024 alloys
In: Engineering Fracture Mechanics (2007) Elsevier

DOI: 10.1016/j.engfracmech.2007.04.008

Anisotropic ductile fracture of Al 2024 alloys

Dirk Steglich[1]♣, Wolfgang Brocks[1], Jürgen Heerens[1], Thomas Pardoen[2]

[1] GKSS Research Centre, Institute for Materials Research, Materials Mechanics, D-21502 Geesthacht, Germany

[2] Department of Materials Sciences and Processes, Université catholique de Louvain, IMAP, Place Sainte Barbe 2, B-1348 Louvain-la-Neuve, Belgium

Abstract

The anisotropic fracture of the 2024-T351 aluminium alloy is investigated using a micromechanics-based damage model accounting for the effect of the void aspect ratio and void distribution. The 2024-T351 Al alloy contains precipitation free bands in which most void nucleating particles are located. The presence of these bands, which are parallel to the rolling direction, primarily controls the distribution of damage and overall fracture anisotropy. The primary void nucleating particles also present a preferential elongation in the rolling direction. These key microstructural features have been determined using quantitative characterization methods. The effect of void shape and void spacing on the fracture behaviour are elucidated by means of FE cell calculations. FE simulations of cylindrical notched round bars loaded in different orientations are made and compared with experimental data, allowing a better understanding of the damage process as well as the limitations of the modeling approach.

Keywords: metals; micromechanics; ductile fracture; void growth; aluminium; anisotropic damage

♣ corresponding author: dirk.steglich@gkss.de

1. Introduction

Airplane designers estimate the residual strength of fuselage components by tests on specimens and components of various sizes. These test campaigns are time consuming and expensive. The development of predictive models for ductile crack extension is thus essential for improving structural design and maintenance, and accelerates the introduction of new materials or assembling methods. Furthermore, fracture mechanics based assessment methods often encounter transferability problems of fracture resistance data from small to large specimens and structures. Micromechanics based damage models such as proposed by Gurson [1], Rousselier [2] or Tvergaard [3] allow capturing the size and geometry effects without the need for introducing extra correction terms such as in the fracture mechanics approach, e.g. for illustration of the methodology [4-9]. In addition, the material parameters can at least partly be identified from investigations of the microstructure, providing the link with processing parameters towards improving materials.

Nevertheless, the currently available models, i.e. the models typically implemented in commercial FE software, are usually restricted to isotropic material behaviour with respect to damage and fracture. Metal alloys, which have undergone extensive plastic deformation by rolling or extrusion, exhibit a significant anisotropy of mechanical properties, however. Even in the case of untextured metals showing isotropic or almost isotropic yielding behaviour, ductility can be very anisotropic, typically with a much smaller value when the loading is applied in the thickness direction due to preferential elongation of the second phase particles responsible for void nucleation. This effect can be considered by orientation dependent damage parameters.

In the present contribution, the model developed by Pardoen and Hutchinson [10-12] based on the growth and coalescence of ellipsoidal voids embedded in a work hardening elasto-plastic matrix material is chosen to simulate the failure of notched round bars made of

Al alloy of the 2024 series. The effect of varying model parameters is studied by cell model calculations. Special emphasis is laid on a careful characterisation of the second phase particles morphology and distribution. From this microstructural information, a simplified model is derived, which allows for directly evaluating model parameters for the loading in S-direction. The loading in the S-direction indeed shows the typical mechanism of growth and coalescence of voids nucleated on primary particles. In a second step, these parameters are identified to predict failure in L-direction which involves a more complex fracture behaviour. The presence in the 2024 alloy of soft Precipitate Free Bands will turn out to be the essential ingredient controlling the ductile fracture process in this material and its anisotropic response. This study is representative of the methodology needed when using micromechanics based approach of fracture requiring in-depth materials characterization to guarantee quantitative predictions and to set the limit of validity of the model.

The paper starts in section 2 with a description of the material, of its microstructure and flow properties. The physics sustaining the constitutive model is briefly described in section 3 while more technical details are given in the Appendix and in the cited references. Section 4 presents the results of FE unit cell calculations which illustrate the importance of the effect of the void distribution and void aspect ratio on the ductility of metallic materials. The identification of the model parameters and the results of the simulations of the cylindrical notched round bars tests performed in two transverse directions are discussed in section 5. The importance of the void distribution is highlighted as well as the limitations of the model.

2. Material and microstructure

The material used in this work is a hot-rolled plate of Al 2024 with a thickness of 100 mm, as received in a T351 temper (solution heat treated, air-quenched, stress-relieved by cold stretching), fabricated several years ago. The main alloying element in the 2XXX series is

copper, while magnesium and manganese are introduced in order to improve the quenching properties. Table 1 summarises the chemical composition of Al 2024.

Table 1. Chemical composition of Al 2024 in wt. %

Cu	Mg	Mn	Si	Fe	Cr
4.11	1.12	0.46	0.048	0.05	0.003

Nucleation takes place either by particle fracture or interface decohesion and sometimes both modes coincide [13-15]. Damage in Al alloys usually nucleates on the large and brittle intermetallic particles (cluster of particles) or coarse precipitates, and sometimes also on smaller particles such as dispersoids or precipitates [14-16]. The morphology and volume fraction of the particles giving rise to voids primarily affect the overall fracture properties. In the specific case of fracture in Al-alloys, damage is essentially induced by the breaking or debonding of coarsened precipitates located inside precipitate free bands, PFB [17]. Optical microscopy, scanning electron microscopy and X-ray microtomography have been used to obtain quantitative information [18] about all these microstructural features. Figure 1a shows a reconstructed view of the investigated volume. The particle clusters appear white, while the surrounding matrix is grey. The particles are aligned in a network-like structure which separates the matrix into domains. The latter have a disc-like shape, with the S-direction as the shortest axis and almost identical dimensions in L- and T-direction, see Fig. 1b.

The fracture mechanisms of the material under investigation depend on the main loading direction. While loading in the S direction, the macroscopic fracture surface is oriented perpendicular to the loading direction (and thus is defined by the LT-plane, see Fig. 2). Any other main loading direction than S (namely L, T and LS) leads to a slanted fracture surface, oriented at 45° with respect to loading direction.

On a microscopic level, the fracture surface resulting with loading in the S-direction shows large broken particles, initiating the void growth process. Grain boundaries are not visible and transgranular fracture is thus dominant, see Fig. 3a. Due to the presence of PFBs, the crack propagates along the weak zones and sometimes jumps along the height of the cluster. This jump can be seen in Fig. 3b by a dashed line, indicating the transition from a focussed region (left) to non-focussed region on a SEM fractography.

When the main loading direction is L (or T), the fracture mode is different from that in S direction. Microscopically, transgranular and intergranular fracture mechanisms are both active for this orientation, see Fig. 4. From the size of the dimples one can presume that void nucleating particles are much smaller than those responsible in S-loading. Thus, a second population of particles, about 20 times smaller than the large particles observed in Fig. 3, are presumably at the origin of the damage process when loading in the L-direction.

A simplified model of this microstructure incorporating the most significant parameters with respect to microstructure and fracture mechanisms has been proposed in [18] and will be applied here. Note that a relatively similar approach has also been used in [19] for a theoretical study of ductile fracture in 7xxx Al alloys with Precipitate Free Zones which are located along grain boundaries. The model assumes that the material is mainly composed of matrix domains surrounded by PFBs containing coarse particles representing the weak regions. Assuming a "closed package" of these matrix domains, the material microstructure can be idealised see Fig. 5, as an assembly of weak and strong layers, 5 μm (average thickness of the PFB) and 25 μm (average thickness of matrix domains) high, respectively. According to this model, loading in the S-direction leads to a high damage rate in the PFB. A macroscopic crack can extend throughout the material perpendicular to the loading direction. For loading in the L-direction, damage will also start in a PFB, but a macroscopic crack will have to cross the tougher matrix material, leading to a higher ductility.

Figure 6a shows the results of the uniaxial tensile tests performed on smooth round bars oriented in L, T and S direction. The plastic anisotropy is quite small when comparing the evolution of the flow stress with plastic deformation while the anisotropy in the fracture strains is very clear: the fracture strain is much lower when loading in the S direction. The limited plastic anisotropy is the result of the lack of pronounced texture. The lower ductility in the S direction can be directly related to the laminated structure as represented in Fig. 5 which provides an easy crack path when loading in the S direction. In the following, test data extracted for tests in L-direction are used to model the work hardening behaviour of the material in all three directions, assuming isotropy with respect to plastic yielding. Fig. 6b depicts the true stress – plastic strain fit, which follows a power law

$$\sigma = \sigma_0 + K\ \varepsilon_{pl}{}^{n}. \tag{1}$$

with a yield stress σ_0 equal to 375 MPa, a strain hardening exponent n equal to 0.67 and a constant K equal to 720.8 MPa.

3. Constitutive anisotropic damage model for ductile fracture

Despite the fact that major efforts have been made over the last decades [1-3] in the modelling of ductile fracture by computational models incorporating the void growth process [4-9], the models currently in use (typically, the models implemented in available commercial FE work packages) suffer from two basic limitations. The first limitation is the assumption of spherical voids growing spherical, preventing to accurately model non-spherical voids as well as void shape changes during deformation. The second limitation is that void coalescence is

only described phenomenologically by an acceleration of damage, which lacks of micromechanical foundation.

Gologanu et al. [20-22] proposed a constitutive relationship for a plastic continuum containing ellipsoidal voids of radii $R_x = R_y$ and R_z. The voids differ according to their aspect ratio, $W = R_z/R_x$ namely: oblate void, $W < 1$, prolate void, $W > 1$, spherical void, $W = 1$. Pardoen and Hutchinson [10-12] extended the Gologanu model by adding a criterion for tensile localisation in the ligament between the voids according to Thomason's approach [23], giving rise to the internal necking mode of coalescence. This criterion requires some assumption on the arrangement of voids in the matrix. Assuming that they are regularly aligned in distances of $2L_x$ and $2L_z$, a representative volume element (RVE) is defined by the aspect ratio, $\lambda = L_z/L_x$. Damage is thus characterised by three parameters, namely the porosity, f, the void shape parameter, W, and the void distribution parameter, λ. A summary of the basic equations of the model is provided in Appendix A while more details can be found in references [10-12] and references cited in the Appendix. The model was implemented in the commercial finite element programme ABAQUS as a user-interface UMAT, as explained in Appendix A.

4. Validation on cell models and single element tests

In order to quantify the effect of initial porosity, stress triaxiality, void shape, and void distribution on void growth and coalescence, a unit cell approach is commonly used [10,24-30]. The continuum is imagined as a periodic array of RVEs, which are assumed to be statistically representative for the microstructure. In particular, a hexagonal cylindrical unit cell containing an ellipsoidal void is considered. For simplicity, the hexagonal cylinder is approximated by a circular cylinder allowing for axisymmetric calculations, and due to

symmetry, only a quarter model has to be considered. The respective FE meshes are embedded in Figs. 7a,b. The geometry of the cell is characterised by three parameters, the initial void volume fraction or "porosity", f_0, the initial void aspect ratio, W_0, and the initial cell aspect ratio, λ_0.

In general, cell model calculations are often used to derive "micromechanical motivated" values for a critical porosity, corresponding to plastic collapse of a cell. Here, the cell calculations are used for two reasons (i): to check the quality of the predictions of the continuum damage model for the specific high strain hardening flow behaviour of the aluminium alloy under investigation, (ii) to motivate and support the analysis of the next section about the effects of the void aspect ratio and void distribution. For the latter, it is well known that hardening affects the collapse characteristic of a cell and thus the point of coalescence.

The cell is subject to axial, u_3, and radial displacements, $u_1 = u_2$. In order to guarantee continuity, the boundaries of the cell are constrained to remain straight and orthogonal during deformation. The "mesoscopic" principal strains, E_i (i = 1, 2, 3), are defined by

$$E_1 = E_2 = \ln\left(1+\frac{u_r}{L_{r0}}\right) \quad ; \quad E_3 = \ln\left(1+\frac{u_z}{L_{z0}}\right) \tag{2}$$

The corresponding "mesoscopic" true principal stresses, $\Sigma_3 \geq \Sigma_1 = \Sigma_2$, are the average reaction forces at the cell boundaries per current areas. The effective stress, Σ_e, and strain, E_e, are calculated from

$$\Sigma_e = \Sigma_3 - \Sigma_1 \quad ; \quad E_e = \tfrac{2}{3}\left|E_3 - E_1\right|. \tag{3}$$

Cell model calculations under monotonous loading are commonly performed at a prescribed fixed stress triaxiality T which is defined as,

$$T = \frac{\Sigma_e}{\Sigma_h} = \frac{3\left(\Sigma_3 - \Sigma_1\right)}{\Sigma_3 + 2\Sigma_1} \quad . \tag{4}$$

The Riks algorithm in the FE-program ABAQUS is usedi n order to prescribe a constant stress triaxiality during the loading process. Elastic properties of the matrix material are assumed to be identical to those of pure aluminium, i. e. E = 70000 MPa, ν = 0.3, and hardening response follows eq. (1) (see also Fig. 6b).

The mechanical response in terms of mesoscopic effective stress vs. mesoscopic effective strain of the cell containing a void is compared with that of the constitutive model, in which case the cell consists of a single element. Fig. 7a comprises results for different values of the void shape parameter, W_0. Model (dashed lines) and unit cell results (solid lines) show the same trends, both in the prediction of maximum load and onset of coalescence. The latter becomes apparent by the sudden drop of the effective stress, which is generally caused by an intervoid necking mechanism in the cell radial direction. For an initially oblate void (W_0 = 1/6), the cell collapses at a much lower effective strain compared to the same cell including a prolate cavity of the same volume. Note that this result is in agreement with the results in [12,31]. As a consequence, elongated voids, $W_0 > 1$, with respect to the main loading direction, weaken a material less and cause delayed fracture compared to oblate ones, if the initial void volume fraction is the same in both cases. Small discrepancies between model and cell predictions are apparent: whereas for initially oblate voids the model predicts earlier coalescence than the cell, it is the opposite for prolate voids.

The effect of different cell aspect ratios, i.e. the spatial void distribution, is displayed in Fig. 7b. Values of λ_0 = 16 (elongated unit cell) and λ_0 = 0.5 (flat unit cell) are chosen as

extreme values. The initial void shape is assumed to be spherical and the ratio of initial void radius and initial cell radius, R_{x0}/L_{x0}, is kept constant, i.e. the radial spacing of the RVEs is the same. As a consequence, the initial void volume fraction varies between 0.00125 ($\lambda_0 = 16$) and 0.04 ($\lambda_0 = 0.5$). An elongated cell causes an earlier collapse compared to a flat one. This phenomenon can be explained by the localisation behaviour of the cells which is promoted by larger stresses on the ligament. In the case of an elongated cell, plastic strain localises in the equatorial plane, leaving a large portion of material "intact". The predictions of the constitutive model (solid lines) reproduce the mechanical response of the unit cells (dashed lines), particularly the dependence of the collapse strain on the aspect ratio, λ_0, is properly captured. For this particular high strain hardening behaviour, void coalescence predicted by the model underestimates the results of the cell calculations, which is opposite to the results shown in [10]. Note that for very low values of λ_0, no coalescence is predicted by the continuum model.

A more general feature of the model is elucidated in Fig. 8: the ability to predict the critical strain of void coalescence, which corresponds to the fracture strain of a material. For the initial volume fraction of $f_0 = 0.01$, the response of the model is compared with a RVE ($W_0=\lambda_0 = 1$) for stress triaxialities T ranging between 0.75 and 5. The well-known dependency of the fracture stain on the triaxiality [38] is well captured by the model. Note that for low triaxialities $T < 0.75$, neither the model nor the cell predicts void coalescence in a realistic range of strain: voids tend to elongate in the loading direction and contract in the transverse direction preventing the internal necking process to set in.

5. Ductile fracture simulations

The constitutive model is now applied to predict damage and fracture of notched round bars with two different notch radii ρ equal to 2 mm and 4 mm, respectively, see specimen geometry in Fig. 9a. The outer and inner diameter are $D = 18$ mm and $d_0 = 10$ mm, respectively. Two specimen orientations, L and S, are considered in the tests and simulations. Micromechanical parameters are taken from the quantitative microstructural analysis. The underlying model of the microstructure is displayed in Fig. 5. The rotational symmetry of the voids with respect to a global axis must be maintained during the whole deformation process. Otherwise, the voids would evolve differently in the two transverse directions. In that case, the model, which considers only spheroidal voids (R_x=R_y) provides an average value of the transverse radius. It is worth noting that, in this geometry, damage is growing faster in the centre of the minimum section where cracking initiation takes place and where a perfectly axisymmetric state of stress is enforced. It is assumed that particles embedded in the soft PFB break or debond in an early stage of deformation and thus nucleate cavities. Any constraint imposed on the void by the embedded particle is ignored (see discussion in [33-35]).

Loading in the S-direction is considered first. A RVE as depicted in the left part of Fig. 5 is assumed. The aspect ratio of the (oblate) cavity can be directly taken from quantitative microstructural analysis, $W_0 = 0.625$. Its shape together with the height of the PFB, $2R_{z0} = 5$ μm, determines the cavity radius, $R_{x0} = R_{z0}/W_0 = 4$ μm. The initial height of the RVE, $2L_{z0}$ (i.e. the mean void spacing in the z-direction) can directly be related to the PFB spacing, $2L_{z0} = 30$ μm. The mean transverse spacing between the voids L_{x0} is estimated from the fracture surface shown in Fig. 3 by taking an average distance between dimple centres and correcting for the transverse strain to obtain the spacing in the undeformed configuration: $2L_{x0} \approx 14$ μm. The RVEs aspect ratio, λ_0, is thus equal to $\lambda_0 \approx 2$. These values give, when

using eqn (A.10) (see Appendix A) with a periodic hexagonal distribution, an initial void volume fraction f_0 equal to 0.031 , in agreement with the microstructural analysis. This result shows that every particle gives rise to a void, otherwise the measured L_{x0} on the fracture surface would have been larger, giving rise a smaller initial void volume fraction.

Transfer of the microstructural information to the simulation of loading in L-direction is not straightforward. The scenarios of choosing a RVE depicted in the right part of Fig. 5 can both apply. Furthermore, other ingredients appear also to control the fracture process, as discussed based on Fig. 4, such as second population of voids and shear driven plastic fracture. Hence, the application of the model in the L loading problem should be considered as phenomenological, and the identification of the λ_0 parameter will be based on fitting one of the notched round bar test (ρ = 2mm was chosen). As shown in Fig. 7b, small values of λ_0 delay coalescence leading to a higher ductility. A value λ_0 = 2 is found here to meet the experimental result. The fact that the value is the same for both L and S orientations is considered to be totally fortuitous. The initial aspect ratio of the void is the inverse of the respective value in S-direction, W_0 = 1.6. The values for f_0, λ_0 and W_0 used in the simulations are summarised in Table 2.

Table 2. Model parameters used in the simulation of fracture of round notched bars

orientation	f_0	λ_0	W_0
S	0.031	2.0	0.625
L	0.031	2.0	1.6

Eight-node isoparametric axisymmetric finite elements were used for the simulations of the tensile tests on notched bars, see Fig. 9b. The yielding behaviour was taken from tensile

tests in L-direction and used for both L- and S-loading case, which means that texture induced plastic anisotropy, is not accounted for as already discussed in Section 2.

Figure 10 comprises the simulation results in terms of applied load vs. reduction of inner diameter, Δd, of the specimens, in comparison to the experimentally obtained fracture points. Four categories of specimens are included: L (open symbols, dashed lines) and S orientation (full symbols and solid lines), notch radius 2mm (circles) and 4 mm (triangles). Due to the higher constraint, the specimens with $\rho = 2$ mm show a higher maximum load. The failure point can be predicted for both specimen orientations, S and L. In the case of $\rho = 4$ mm, the simulation result obtained for S-direction meets the experiments, whereas the ductility in L-direction is still significantly overestimated by the simulation.

For both S and L directions, the effect of the stress triaxiality on the fracture strain is quite small compared to the traditional and well accepted view since the pioneering works by Rice and Tracey [36], Mc Clintock [37] and Hancock and McKenzie [38], see also the results of Fig. 8. A different explanation is forwarded for each orientation. In the case of the S direction, the presence of harder zones around the soft precipitate free bands induces an extra constraint which superimposes on the applied stress triaxiality. This extra constraint can be quite high, see [19], and dominate the stress state, resulting in an apparently limited effect of the stress triaxiality. This extra constraint effect is not incorporated in the present implementation of the model which can also explain why the predictions under uniaxial tension markedly underestimate the ductility. Indeed, as shown in Fig. 8, a small stress triaxiality typical of uniaxial tension with necking, very small changes of the stress triaxiality induce major changes in the fracture strain. This explains also why simulations of the fracture of smooth round bars loaded in S-direction, not reported in the paper, have not been successful. In the experiment, the specimens failed without showing any significant necking. In the case of the L direction, we believe that the intrinsic fracture mechanism involving intergranular fracture and second population of voids is not much controlled by the classical

void growth stage but by void nucleation events and shear localization process which are less sensitive to stress triaxiality.

6. Conclusions

The fracture behaviour of metal sheets generally depends on the loading direction even in the absence of significant crystallographic textures. In many instances, the ductility is reduced when the sample is deformed in the thickness direction due to a preferential orientation of elongated second phase particles in the rolling direction. A second effect which adds to this morphological controlled anisotropy is the clustering of the particles into long bands providing an easy percolating crack path. The material investigated in this study, the Al 2024 alloy, exhibits both effects.

An idealised axisymmetric periodic microstructure has been assumed which incorporates the most significant features determined from quantitative characterization. The effects of stress triaxiality, void shape, and void distribution on the growth and coalescence process have been studied by means of FE cell calculation. The results, showing the first order influence of both the void shape and void distribution, have been compared with the predictions of a micromechanical based damage model. The constitutive model has been applied to simulate the failure behaviour of cylindrical notched bars. The model parameters for loading in S-direction are directly obtained from the microstructural analysis while the application in the L-direction required some empirical adjustment. The model is able to reproduce the ductility anisotropy and part of the stress triaxiality dependence. Nevertheless, this application demonstrates also the need for extra efforts in the development of micromechanical models including physical processes of two main kinds, namely:

1. the necessity to introduce, when required, an intermediate scale between the voids level and the macroscopic level. This intermediate scale in the present material consists of soft precipitate free bands in which all primary particles are located. Other example of meso-heterogeneities are given by welded joints, multiphase alloys, grain boundary precipitate free zones, graded ductile materials,
2. the micromechanical treatment of shear driven ductile fracture process in which the main controlling damage mechanism is not the classical nucleation, growth and coalescence of primary voids.

Acknowledgements

The experimental part of this program was supported by the Deutsche Forschungsgemeinschaft within the Collaborative Research Centre "Micromechanics of Multiphase Materials" (SFB 371). The authors acknowledge the financial support as well as the valuable input of D. Paganelli and G. Quan.

References

[1] Gurson AL. Continuum theory of ductile rupture by void nucleation and growth: Part I-Yield criteria and flow rules for porous ductile media. J Engng Mater Tech 1977; 99:2-15.

[2] Rousselier G. Ductile fracture models and their potential in local approach of fracture. Nucl Eng Des 1987;105: 97-111.

[3] Tvergaard V. Material failure by void growth to coalescence. Adv Appl Mech 1990; 27: 83-151.

[4] Brocks W, Klingbeil D, Künecke G and Sun D.-Z. Application of the Gurson model to ductile tearing resistance. 1995; Constraint Effects in Fracture Theory and Applications: Second Volume, ASTM STP 1244; eds Kirk M. and Bakker A. 232-252.

[5] Tvergaard V and Needleman A. Analysis of the cup and cone fracture in a round tensile bar. Acta Metall 1984; 32: 157-169.

[6] Chabanet O, Steglich D, Besson J, Heitman V, Hellmann D and Brocks W. Predicting crack growth resistance of aluminium sheets. Compt Mater Sci 2003; 26: 1-12.

[7] Devaux J.C, Mudry F, Pineau A, and Rousselier G. Experimental and numerical validation of a ductile fracture local criterion based on a simulation of cavity growth. 1989, In: "Non Linear Fracture Mechanics: Volume II – Elastic-Plastic Fracture", ASTM STP 995, eds. J.D. Landes, A. Saxena and J.G. Merkle. 7-23.

[8] Ruggieri C, Panontin T.L, and Dodds Jr. R. H. Numerical modeling of ductile crack growth in 3-D using computational cell elements. Int J Fract 1996; 82: 67-95.

[9] Xia L, Shih C and Hutchinson J. A computational approach to ductile crack growth under large scale yielding conditions. J Mech Phys Solids 1995; 43: 389–413.

[10] Pardoen T, Hutchinson JW. An extended model for void growth and coalescence. J Mech Phys Solids 2000;48:2467-2512.

[11] Pardoen T, Hutchinson JW. Micromechanics-based model for trends in toughness of ductile metals. Acta Mater 2003;51:133-148.

[12] Pardoen T. Numerical simulation of low stress triaxiality ductile fracture. Computers and Structures 2006; 84:1641-1650.

[13] Beremin FM. Cavity formation from inclusions in ductile fracture of A508 steel. Metall Trans A 1981;12:723-731.

[14] Pardoen T, Pineau A. Failure Mechanisms of Metals. In Comprehensive Structural

Integrity Encyclopedia, Elsevier, Vol 2, Chapter 6 (2007).

[15] Lassance D, Fabrègue D, Delannay F, and Pardoen T. Micromechanics of room and high temperature fracture in 6xxx Al alloys. Progress in Materials Science 2007; 52:62-129.

[16] Garrett G.G and Knott J.F. The influence of compositional and microstructural variations on the mechanism of static fracture in aluminium alloys. Metallurgical Transactions A 1978; 9A:1187-1201.

[17] M. de Hass M. and De Hosson J.Th.M. Grain boundary segregation and precipitation in aluminium alloys, Scripta Materialia 2001;44: 281-286.

[18] Quan G, Heerens J, and Brocks W. Distribution characteristics of constituent particles in thick plate of 2024 Al-T351, Prakt Metallogr 2004; 41:304-313.

[19] Pardoen T, Dumont D, Deschamps A, Brechet Y. Grain boundary versus transgranular ductile failure. J Mech Phys Solids 2003; 51:637-665.

[20] Gologanu M, Leblond J.B, and Devaux J. Approximate models for ductile metals containing non spherical voids - case of axisymmetric prolate ellipsoidal cavities. J Mech Phys Solids 1993; 41:1723-1754.

[21] Gologanu M, Leblond J.-B, and Devaux J. Approximate models for ductile metals containing non-spherical voids – case of axisymmetric oblate ellipsoidal cavities. ASME. J Eng Mater Technol 1994; 116: 290–297.

[22] Gologanu M, Leblond J.-B, Perrin G, and Devaux J. Recent extensions of Gurson's model for porous ductile metals 1997, In: "Continuum Micromechanics". CISM Lectures Series, ed. P. Suquet. Springer, New York, 61–130.

[23] Thomason P. F. Ductile Fracture of Metals, Pergamon Press (1990).

[24] Koplik J, Needleman A. Void growth and coalescence in porous plastic solids. Int J Solids Struct 1988;24:835-853.

[25] Brocks W, Sun DZ, Hönig A. Verification of the transferability of micromechanical parameters by cell model calculations with visco-plastic materials. Int J Plast 1995;11:971-989.

[26] Kuna M, Sun DZ. Three-dimensional cell model analyses of void growth in ductile materials. Int J Fract 1996;81:235-258.

[27] Needleman A. Void growth in an elastic-plastic medium. J Appl Mech 1972;39:964-970.

[28] Tvergaard V. Influence of voids on shear band instabilities under plane strain conditions. Int J Fract 1981;17:389-407.

[29] Hom CL, McMeeking RM. Void growth in elastic-plastic materials. J Appl Mech 1989;56:309-317.

[30] Kim J, Gao XS, Joshi S. Modeling of void growth in ductile solids: effects of stress triaxiaility and initial porosity. Engng Fract Mech 2004;71:379-400.

[31] Sovik O. P, and Thaulow C. Growth of spheroidal voids in elastic-plastic solids. Fat Fract Eng Mater Struct 1997;20: 1731-1744.

[32] Hancock J.W, and Cowling M.J. Role of state of stress in crack-tip failure processes, Metal Science 1980, 293-304.

[33] Steglich D, Brocks W. Micromechanical modeling of the behavior of ductile materials including particles. Comput Mater Sci 1997;9:7-17.

[34] Siruguet K, Leblond J-B. Effect of void locking by inclusions upon the plastic behavior of porous ductile solids - I: theoretical modeling and numerical study of void growth. Int J Plast 2004;20:225-54.

[35] Maire E, Bordreuil C, Babout L, and Boyer J. C. 2005, Damage initiation and growth in metals. Comparison between modeling and tomography experiments. J. Mech. Phys. Solids; 53: 2411-2434.

[36] Rice J.R and Tracey D.M. On the ductile enlargement of voids in triaxial stress fields. J Mech Phys Solids 1969;17:201-217.

[37] McClintock F. A. A criterion for ductile fracture by the growth of holes. J Appl Mech 1968; 35: 363-371.

[38] Hancock J.W. and A.C. Mackenzie. On the mechanisms of ductile failure in high-strength steels subjected to multi-axial stress-states. J Mech Phys Solids 1977; 14: 147-169.

[39] Benzerga A and Besson J. Plastic potentials for anisotropic porous solids. Eur J Mech 2001; 20A, 3, 397–434.

[40] Benzerga A Besson J and Pineau A. Anisotropic ductile fracture – Part II: theory. Acta Mater 2004; 52: 4639-4650.

[41] Huber G Brechet Y and Pardoen T. Void growth and void nucleation controlled ductility in quasi eutectic cast aluminium alloys. Acta Mater 2005; 53, 2739-2749.

[42] Lassance D Scheyvaerts F and Pardoen T. Growth and coalescence of penny-shaped voids in metallic alloys. Eng Fract Mech 2006; 73: 1009-1034.

[43] Scheyvaerts F Onck P Bréchet Y and Pardoen T. Multiscale simulation of the competition between intergranular and transgranular fracture. Proceedings of ICF11 – 11th International Conference on Fracture 2005, CD-Rom.

[44] Eshelby JD. The determination of the elastic field of an ellipsoidal inclusion and related problems. Proc Roy Soc London, Ser. A 1957;241:376-396.

[45] Mori T Tanaka K. Average stress in matrix and average elastic energy of materials with misfitting inclusions. Acta Metall 1973; 21:571-574.

Appendix A – Brief description of the extended Gurson model

An extension of the Gurson model [1] based on the contributions by Gologanu *et al.* [20-22] and Thomason [23] and accounting for the effect of the growth and coalescence of *spheroidal* voids[1] on the behaviour of the material has been presented by Pardoen and Hutchinson [10-12]. The response of the matrix is assumed to obey J2 flow theory. Plastic anisotropy of the matrix can be introduced following the framework proposed by Benzerga and co-workers [39,40]. The version of the model presented here considers the voids present from the beginning of the deformation history which is a good approximation for many materials. Void nucleation models can be readily incorporated into the present constitutive model (see for instance [41,42]).

The model is based on two solutions for the expansion of a void in an elasto-plastic material : one solution is called "void growth" corresponding to diffuse plasticity around the void, and the other is called "void coalescence" corresponding to localized plasticity in the ligament between the growing voids. These two solutions are cast in the form of two distinct plastic yield surfaces supplemented by the normality rule for the plastic strain increments and evolution laws for the internal variables: porosity f, void aspect ratio W (or $S \equiv \ln W$), relative void spacing χ (void diameter divided by void spacing), and mean yield stress of the matrix material σ_y:

Yield surfaces

Growth:

$$\Phi_{\text{growth}} \equiv \frac{C}{\sigma_y^2}\left\|\boldsymbol{\sigma}'+\eta\sigma_{\text{h}}^{\text{g}}\boldsymbol{X}\right\|^2 + 2q(g+1)(g+f)\cosh\left(\kappa\frac{\sigma_{\text{h}}^{\text{g}}}{\sigma_y}\right)-(g+1)^2-q^2(g+f)^2=0 \quad \text{(A.1)}$$

Coalescence:

$$\Phi_{\text{coalescence}} \equiv \frac{\|\boldsymbol{\sigma}'\|}{\sigma_y}+\frac{3}{2}\frac{|\sigma_h|}{\sigma_y}-F(W,\chi)=0 \quad \text{(A.2)}$$

$$\text{with } F(W,\chi)=\frac{3}{2}(1-\chi^2)\left[\alpha\left(\frac{1-\chi}{\chi W}\right)^2+\beta\sqrt{\frac{1}{\chi}}\right] \quad \text{(A.3)}$$

[1] A spheroid is an ellipsoid with a symmetry of revolution around one axis.

Evolution law for *f*

Growth and coalescence : $$\dot{f} = (1-f)\dot{\varepsilon}^p_{kk} \tag{A.4}$$

Evolution law for *W (or S = lnW)*

Growth : $$\dot{S} = \frac{3}{2}(1+h_1)\left(\dot{\boldsymbol{\varepsilon}}^p - \frac{\dot{\varepsilon}^p_{kk}}{3}\boldsymbol{\delta}\right) : \boldsymbol{P} + h_2\dot{\varepsilon}^p_{kk} \tag{A.5}$$

Coalescence : $$\dot{W} = \frac{W\left(2\chi^2-1\right)}{2f}\left[\frac{3}{2}\dot{\boldsymbol{\varepsilon}}^p : \boldsymbol{P} - \frac{1}{2}\dot{\varepsilon}^p_{kk}\right] \tag{A.6}$$

Evolution laws for σ_y

Growth : $$\sigma_y\,\dot{\varepsilon}^p_y(1-f) = \boldsymbol{\sigma} : \dot{\boldsymbol{\varepsilon}}^p \tag{A.7}$$

Coalescence : $$\dot{\sigma}_y = \frac{\partial\sigma_y}{\partial\varepsilon^p_y}\frac{\chi^2}{f}\dot{\varepsilon}^p_e \tag{A.8}$$

Evolution for χ

Coalescence : $$\dot{\chi} = \frac{\chi\left(3-2\chi^2\right)}{6f}\left[\frac{3}{2}\dot{\boldsymbol{\varepsilon}}^p : \boldsymbol{P} - \frac{1}{2}\dot{\varepsilon}^p_{kk}\right] \tag{A.9}$$

In Eqs. (1) to (9),

- The first yield surface Φ_{growth} is a Gurson-type yield surface derived by Gologanu-Leblond-Devaux for spheroidal voids [20-22] and extended to strain hardening materials [10]. The yield function $\Phi_{coalescence}$ has been developed in the spirit of the work by Thomason [23], extended to the full coalescence response and to strain hardening materials.
- $\boldsymbol{\sigma}$ is the Cauchy stress tensor; $\boldsymbol{\sigma}'$ is the deviatoric part of the Cauchy stress tensor; σ_h^g is a generalized hydrostatic stress defined by $\sigma_h^g = \boldsymbol{\sigma} : \boldsymbol{J}$.
- $\boldsymbol{X}$ is a tensor associated to the void axis and defined by 2/3 $\boldsymbol{e}_z\otimes\boldsymbol{e}_z$-1/3 $\boldsymbol{e}_x\otimes\boldsymbol{e}_x$-1/3 $\boldsymbol{e}_y\otimes\boldsymbol{e}_y$ ($\boldsymbol{e}_z$ is the base vector parallel to the cavity axis); $\boldsymbol{J}$ is a tensor associated to the void axis and defined by (1-2α_2)$\boldsymbol{e}_z\otimes\boldsymbol{e}_z$+ $\alpha_2\boldsymbol{e}_x\otimes\boldsymbol{e}_x$+ $\alpha_2\boldsymbol{e}_y\otimes\boldsymbol{e}_y$; $\boldsymbol{P}$ is a projector tensor, defined by $\boldsymbol{e}_z\otimes\boldsymbol{e}_z$; $\boldsymbol{\delta}$ is the Kronecker tensor.

- The symbol $\| \ \|$ represents the von Mises norm.
- Gologanu *et al*. [20-22] derived analytical relationships for the dummy parameters C, η, g, κ, h_1, h_2, α_2 in terms of the state variables W and f (see also [10] for full expression).
- The parameter q has been calibrated as a function of f_0, W_0, and the mean strain hardening capacity of the material (exponent n in equation (A.16) next) (see [10] for complete expressions); α has been calibrated as a function of the mean strain hardening index n : $\alpha = 0.1+0.217n+4.83n^2$, see [10]; β is equal to 1.24.
- The plastic strain rate tensor $\dot{\boldsymbol{\varepsilon}}^p$ is defined in the reference configuration; $\dot{\varepsilon}_e^p$ is the equivalent plastic strain rate (or accumulated plastic strain rate); $\dot{\varepsilon}_y^p$ is the equivalent plastic strain rate of the matrix material. The effective plastic strain of the matrix material ε_y^p is related to the current yield stress of the matrix material σ_y through the material true stress true strain curve, see later eqn (A.16).

The response of the material under loading is first elastic while the stress state lies within the elastic domain of the two yield surfaces. In the beginning of the deformation, the voids are small and the spacing is large resulting in a diffuse mode of plastic deformation. Except for pathological cases, the first yield surface to be reached is thus Φ_{growth}. With increasing deformation Φ_{growth} first expands due to hardening and then contracts due to damage softening. Void growth and ligament reduction also induce contraction of $\Phi_{\text{coalescence}}$. When the two yield surfaces intersect at the current loading point, transition to coalescence occurs. With increasing deformation the coalescence yield surface rapidly contracts towards the zero stress state.

Note that the parameter χ does not affect the void growth response. It is calculated during the void growth phase only to test the condition of coalescence using the following geometrical relationship:

$$\chi = \left(\frac{f\lambda}{\gamma_g W} \right)^{\frac{1}{3}} \tag{A.10}$$

where λ is equal to $2\ L_z/(L_x+ L_y)$ and L_x, L_y and L_z are the mean void spacings in the three directions corresponding to the three void axis (whose evolution can directly be obtained from the strains in the corresponding directions), and γ_g is a geometric factor which depends on the void distribution. In the case of periodic packing of voids, $\gamma_g = \pi/6 = 0.523$ for a simple cubic array, $\gamma_g = \sqrt{3}\pi/9 = 0.605$ for an hexagonal distribution and $\gamma_g = 2/3 = 0.666$ for a void surrounded by a cylindrical matrix.

The model is completed by the normality rule for the plastic strain increment and an evolution law for the void axis

$$\dot{\varepsilon}_{ij}^{p} = \dot{\gamma}\frac{\partial \Phi}{\partial \sigma_{ij}}, \tag{A.11}$$

$$\dot{\boldsymbol{e}}_{\boldsymbol{z}} = \boldsymbol{\Omega}\boldsymbol{e}_{z}, \tag{A.12}$$

where the spin tensor $\boldsymbol{\Omega}$ is taken here as the material spin tensor. The voids are thus assumed to rotate with the material. This is the assumption also proposed by Gologanu [20-22]. A more accurate void rotation law, motivated by 3D finite element void cell calculations, as been recently developed (see [43] in which a modified version of the coalescence model is also introduced).

Isotropic elasticity is assumed while using the Eshelby [44] - Mori-Tanaka [45] homogenization method to approximately couple the elastic constants to the porosity (spherical voids approximation):

$$K = \frac{4(1-f)K_0G_0}{4G_0 + 3fK_0}, \tag{A.13}$$

$$G = \frac{(1-f)G_0}{1+\dfrac{f(6K_0+12G_0)}{9K_0+8G_0}} \tag{A.14}$$

where G and K are the overall shear and bulk moduli, respectively and G_0 and K_0 are the shear and bulk moduli of the undamaged material, respectively.

Finally, the following uniaxial response has been chosen :

$$\frac{\sigma}{\sigma_0} = \frac{E\varepsilon}{\sigma_0} \quad \text{when } \sigma < \sigma_0 \,, \tag{A.15}$$

$$\sigma = \sigma_0 + K\varepsilon^{p^n} \quad \text{when } \sigma > \sigma_0 \ . \tag{A.16}$$

The constitutive model has been implemented in the finite element program "ABAQUS Standard" through a User defined MATerial subroutine. Details about the implementation of the two parts of the constitutive models can be found in ref [12].

Tables and table captions

Table 1. Chemical composition of Al 2024 in wt. %

Cu	Mg	Mn	Si	Fe	Cr
4.11	1.12	0.46	0.048	0.05	0.003

Table 2. Model parameters used in the simulation of fracture of round notched bars

orientation	f_0	λ_0	W_0
S	0.031	2.	0.625
L	0.031	2.0	1.6

Figure captions

Figure 1. (a) Particle clusters (white) in the investigated material in an XDM analysis, (b) Matrix domains surrounded by weak precipitate free bands

Figure 2. Macroscopic orientation of fracture surfaces in dependence of the main loading direction

Figure 3. Fracture surface (LT-plane) with S as the main loading direction showing transgranular ductile fracture. The dashed line indicates a "jump" of the crack path, leading to a "step" in the LT-pane

Figure 4. Fracture surface (45° inclined w. r. t. the SL-plane) with L as the main loading direction. The numbers correspond to intergranular ductile fracture (1) and transgranular ductile fracture (2) regions.

Figure 5. Simplified model of the microstructure, choice of the RVE

Figure 6. Results of the tensile tests: Force - elongation (a) and true stress – plastic strain data

Figure 7. Mesoscopic response of a unit cell with void in comparison with the GPH model prediction, for $T = 1$, $f_0 = 10^{-4}$: (a) Effect of the void shape, W_0, $\lambda_0 = 1$; (b) Effect of the cell aspect ratio, λ_0, spherical void ($W_0 = 1$), $R_{r0}/L_{r0} = 0.3$

Figure 8. Critical mesoscopic strains: prediction of the GPH model and of a unit cell for $f_0 = 10^{-2}$, $W_0 = \lambda_0 = 1$

Figure 9. Round notched bars (d_0=4 mm, D_0=10 mm, ρ=2 and 4 mm): (a) specimen geometry; (b) axisymmetric FE meshes

Figure 10. Macroscopic specimen behaviour

Figures

(a) 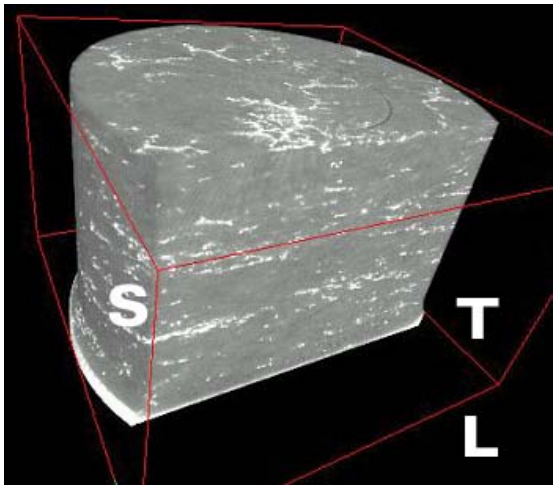

(b) 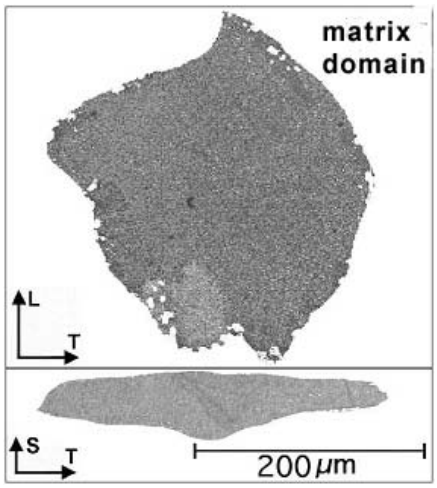

Figure 1. (a) Particle clusters (white) in the investigated material in an XDM analysis, (b) Matrix domains surrounded by weak precipitate free bands

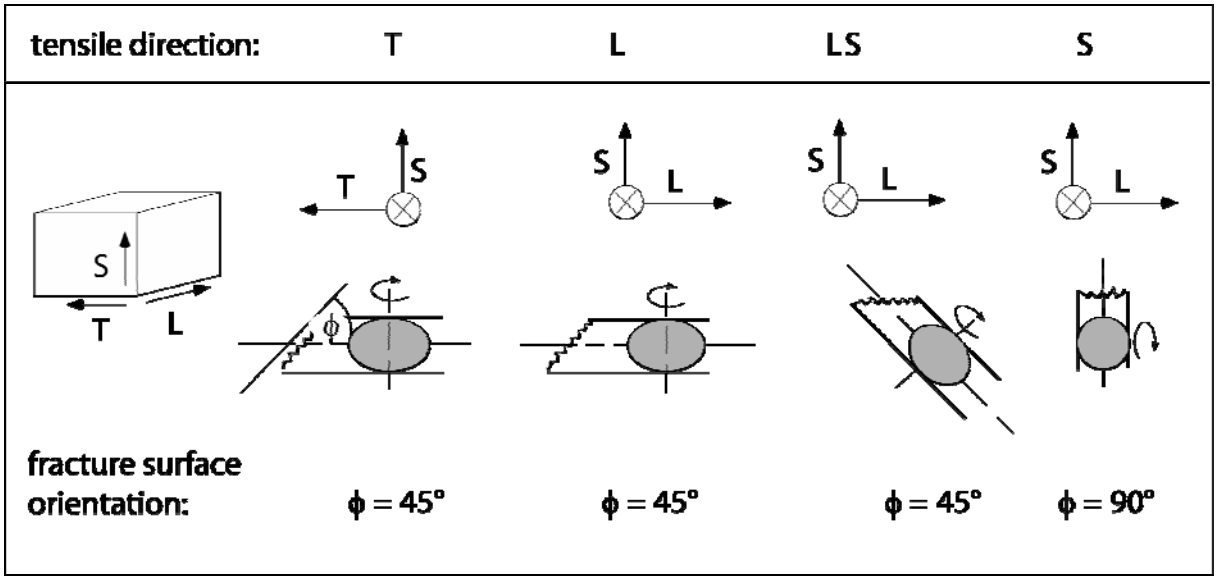

Figure 2. Macroscopic orientation of fracture surfaces in dependence of the main loading direction

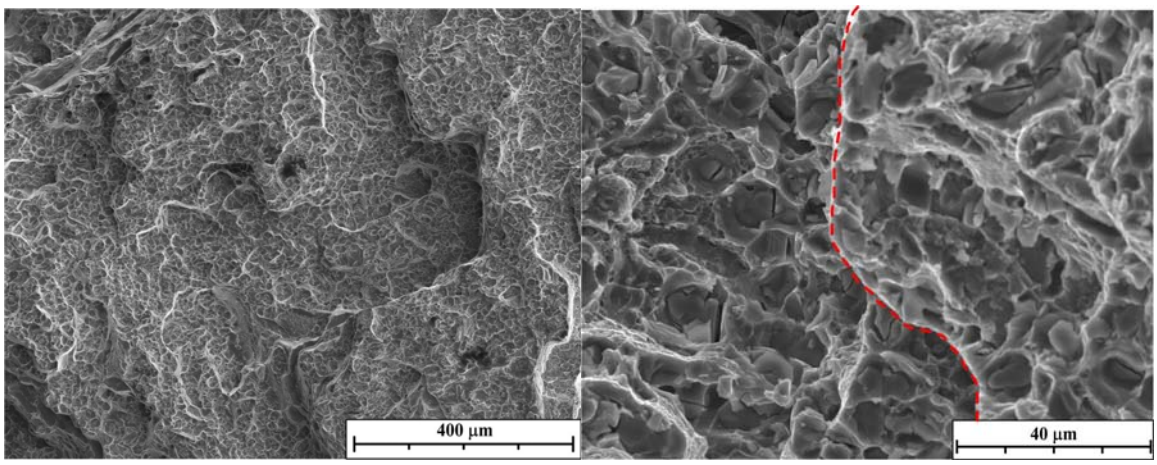

Figure 3. Fracture surface (LT-plane) with S as the main loading direction showing transgranular ductile fracture. The dashed line indicates a "jump" of the crack path, leading to a "step" in the LT-pane

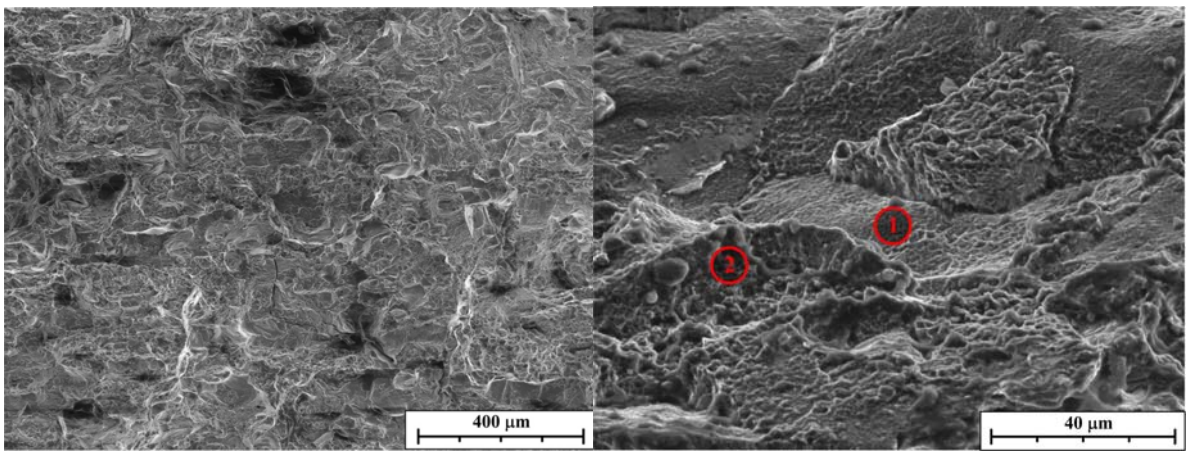

Figure 4. Fracture surface (45° inclined w. r. t. the SL-plane) with L as the main loading direction. The numbers correspond to intergranular ductile fracture (1) and transgranular ductile fracture (2) regions.

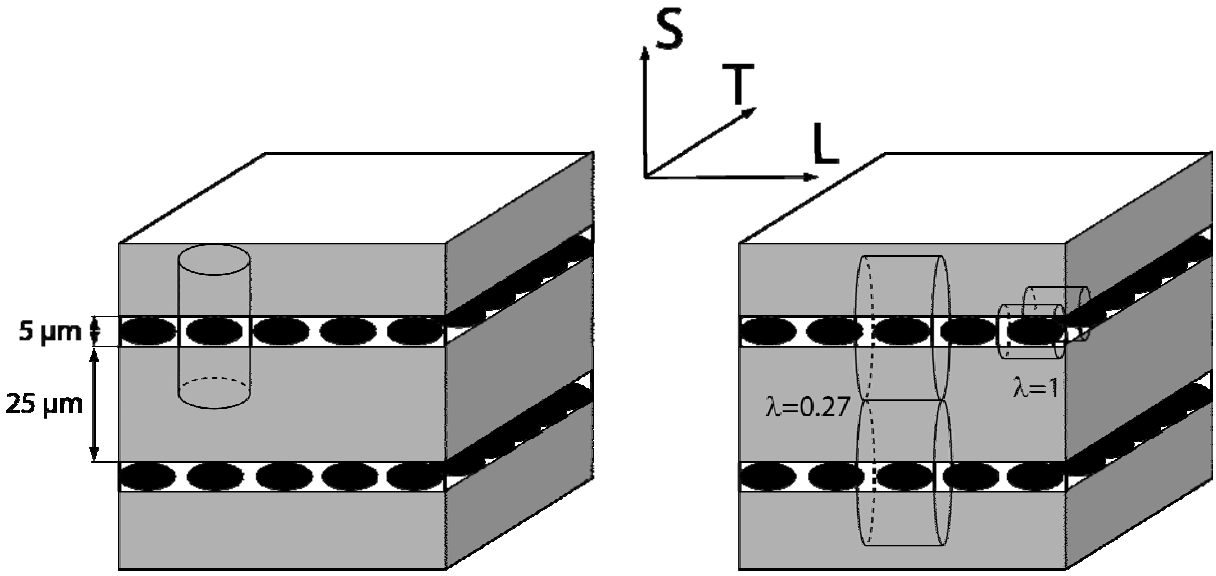

Figure 5. Simplified model of the microstructure, choice of the RVE

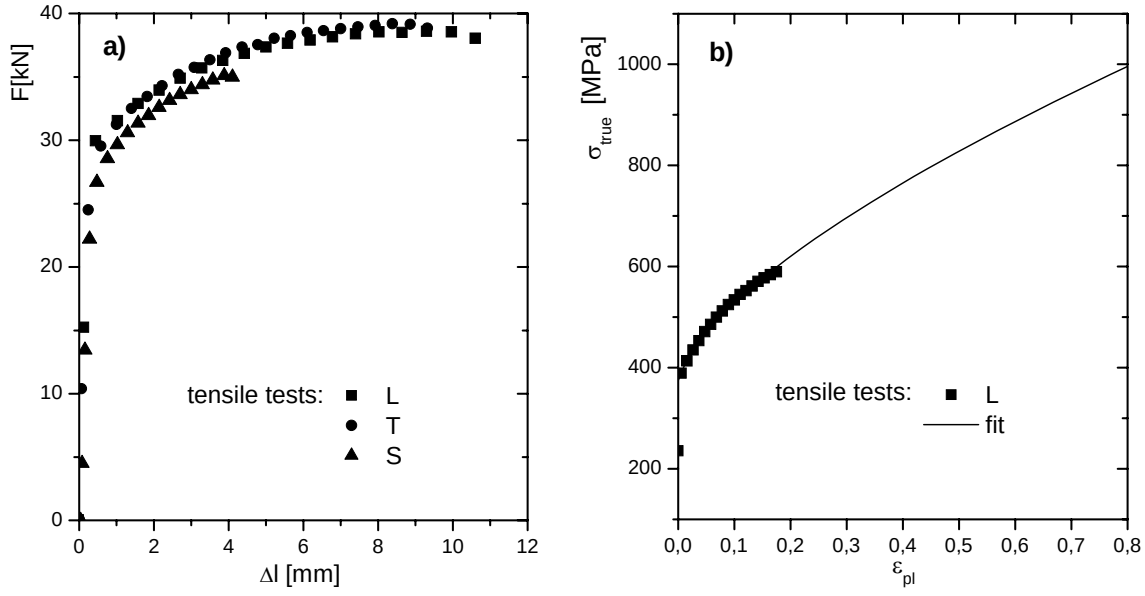

Figure 6. Results of the tensile tests: Force - elongation (a) and true stress – plastic strain data (b)

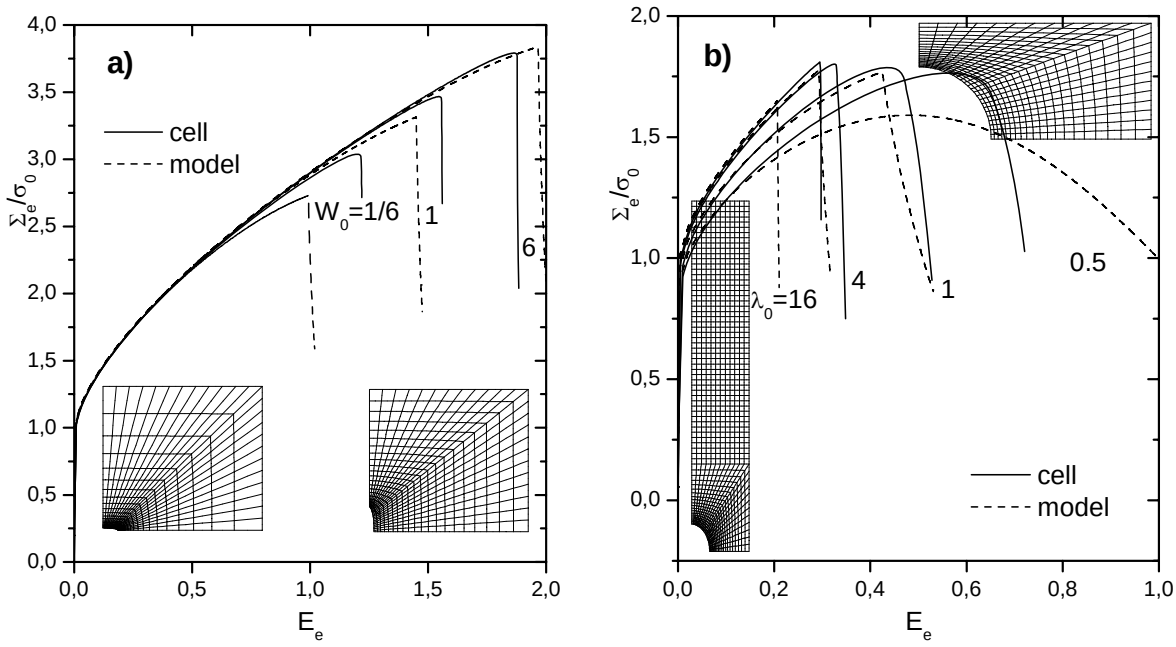

Figure 7. Mesoscopic response of a unit cell with void in comparison with the GPH model prediction, for $T = 1$, $f_0 = 10^{-4}$: (a) Effect of the void shape, W_0, $\lambda_0 = 1$; (b) Effect of the cell aspect ratio, λ_0, spherical void ($W_0 = 1$), $R_{r0}/L_{r0} = 0.3$

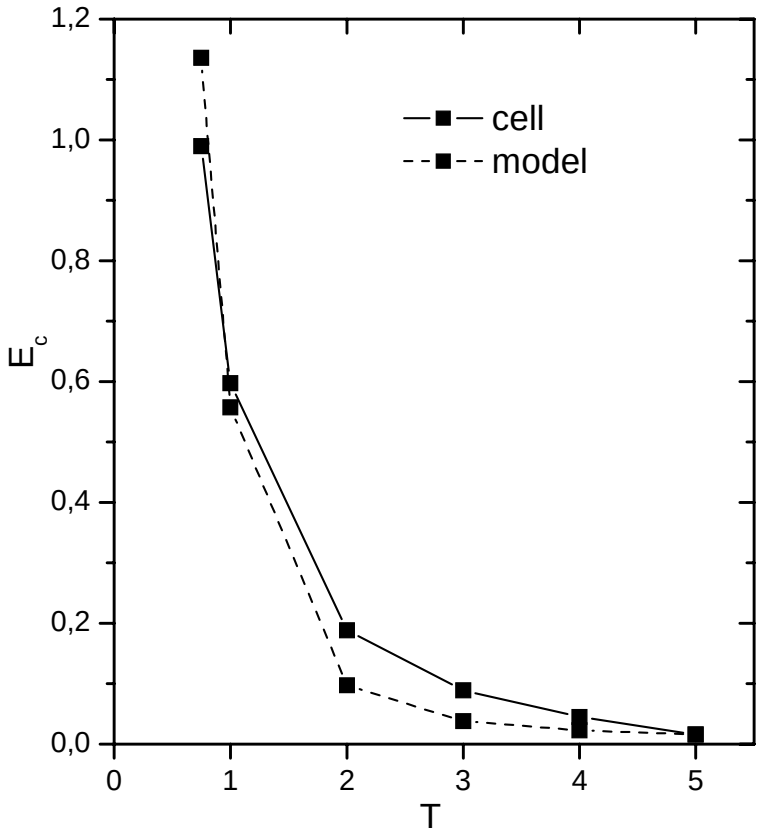

Figure 8. Critical mesoscopic strains: prediction of the GPH model and of a unit cell for $f_0 = 10^{-2}$, $W_0=\lambda_0 = 1$

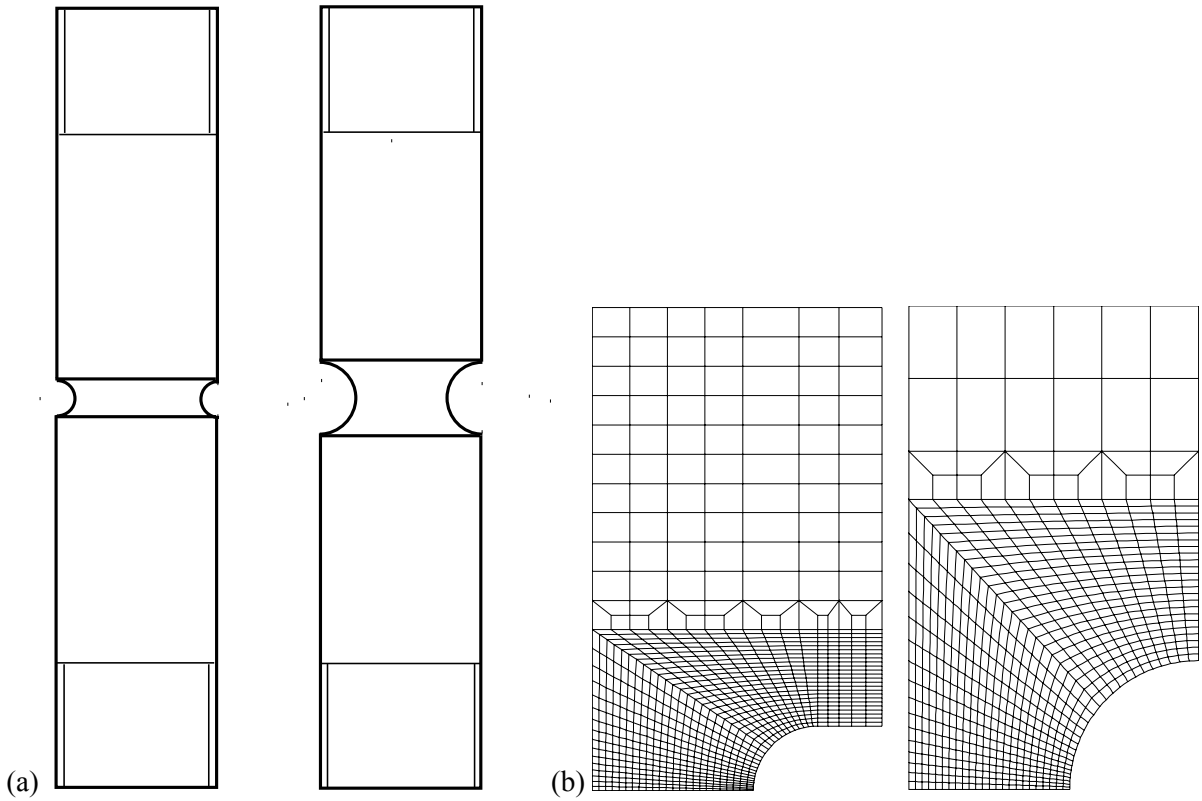

Figure 9. Round notched bars (d_0=4 mm, D_0=10 mm, ρ=2 and 4 mm): (a) specimen geometry; (b) axisymmetric FE meshes

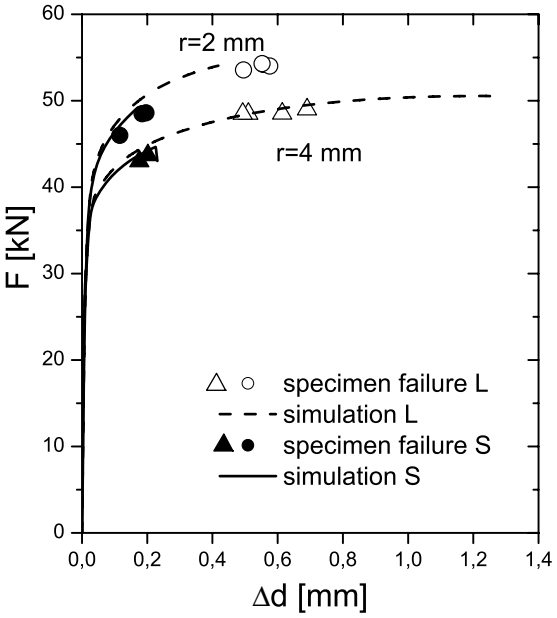

Figure 10. Macroscopic specimen behaviour